# Co single atom modulating the secondary coordination environment of Bi sites for boosting the adsorptive and catalytic capacity during CO₂ photoreduction

Yong Xu [a], Man Zhang [a], Jianfei Long [a], Weili Dai [a,*], Ping Wang [a], Lixia Yang [a], Jianping Zou [a], Xubiao Luo [a,b]

[a] *Key Laboratory of Jiangxi Province for Persistent Pollutants Control and Resources Recycle, Nanchang Hangkong University, Nanchang 330063, PR China*
[b] *School of Life Science, Jinggangshan University, Ji'an 343009, PR China*

ARTICLE INFO

ABSTRACT

In this work, a promising strategy was established to regulate the coordination environment of Bi active sites through metal atom doping. Interestingly, the doped Co in BiO quantum dots (QDs) are atomically dispersed in the second coordination shell, and can promote the hybridization and redistribution of atomic orbitals, thus improving the interaction with C 2p orbital in CO₂ molecules. The Co single atom located at the secondary coordination shell changes the work function of BiO QDs, thereby facilitating the transfer of photogenerated electrons from Co to Bi active sites, and thus more long-lived electrons can take part in the CO₂ reduction reaction. Additionally, the free energy calculations demonstrate that the existence of Co single atoms in secondary coordination environment is conducive to reduce the formation energy barriers as well as boost the stability of the intermediate *COOH, thus promoting the catalytic performance towards CO₂ reduction.

## 1. Introduction

Nowadays, more than 80% of the energy needed for human production and life is provided by fossil fuel combustion [1], which inevitably leads to a large amount of CO₂ emissions, thus resulting in a serious of problems, such as frequent extreme weather, ecosystem damage, sea level rise, food shortage and so on [2,3]. At present, one of the best way to achieve carbon neutrality is to convert CO₂ into high added-value compounds driven by sunlight, which reduces the concentration of CO₂ by simulating natural photosynthesis [4]. However, the CO₂ molecules contain strong C=O double bonds (750 kJ/mol), and the conjugative effect of two C=O bonds leads to the double bond exhibiting some properties of triple bond [5,6]. Therefore, the activation of CO₂ molecule is a major problem in its catalytic reduction, which needs up to − 1.9 V (vs normal hydrogen electrode, NHE) in theory to produce carbon dioxide anion radical (CO₂⁻) [7]. On the other hand, multifarious products can be obtained after CO₂ reduction, such as CO, HCOOH, HCHO, CH₃OH, CH₄ and C₂H₄, etc, and thus the subsequent separation and purification of the mixture is unfavorable for industrial production [8]. Accordingly, the design and development of photocatalysts with

high CO₂ reduction activity as well as high product selectivity is the only way to solve the issue of difficult activation of CO₂ and promote the directional generation of reduction products. It is well known that the most critical step of fabricating a high efficient catalyst is to construct and regulate the catalytic active sites, which have an important influence on the adsorption, activation, catalytic reaction path and product desorption [7–12].

Strenuous efforts have been made to improve the ability of photocatalyst to activate CO₂ molecules, such as interface engineering, polarization engineering, manufacturing defects, constructing amorphous surface, fabricating single atom catalyst and so on [9–17]. Whereas the essence of these strategies is to improve the transfer rate and separation efficiency of photogenerated electrons, change the active sites or regulate the microenvironment of active sites. Among them, manipulating the microenvironment is to alter the catalytic activity, reaction path and product selectivity by modulating the coordination environment of the active site without changing the inherent active site, which may be beneficial for the inherent adsorption and activation of reactant molecules. Li et al. obtained Co-based catalysts with different number of N coordination atoms by calcining the precursors at different

* Corresponding author.
*E-mail address:* wldai81@126.com (W. Dai).

temperatures, and the evolution rate of CO derived from $CO_2$ reduction is significantly increased by the Co atom coordinated with two N atoms [18]. In addition to the influence of the first-shell coordination atoms on catalytic active sites, the second-shell of atoms can also regulate the catalytic performance. Xin et al. prepared the precursor by mixing sulfur and MOF (metal organic framework) in mixture solvent, which was calcined to obtain Ru-based catalyst (Ru-N$_4$) with S atom replacing C atom on the second shell [19]. The S at the second shell could modify the *d*-orbital electrons of Ru to lower the energy barrier of intermediates, thus boosting oxygen reduction activity. Xiang et al. reported that the interactions between the single atoms of Co and Ru increased the adsorption capacity of $CO_2$ molecules, thereby improving catalytic efficiency and achieving high turnover number [20]. Consequently, the microenvironment of active sites is one of the crucial factors to affect the adsorption and activation of reactant molecules as well as the selectivity of products [21]. And corresponding research is needed to deeply carry out in the field of photocatalytic $CO_2$ reduction.

The low-valent metal in semiconductor material possesses fewer coordination atoms than corresponding metal in high-valent state, and is hence coordinatively unsaturated, which is favorable to stimulate the adsorption and activation of $CO_2$ molecules. However, there is limited research on the photoreduction of $CO_2$ by low-valent metal compounds, which may be due to the instability of such semiconductors like SnO. The second case is that the conduction band (CB) potential of stable $W_{18}O_{49}$ is 0.13 V, which does not meet the requirement ($\leq -0.53$ V). Strikingly, low-valence BiO is a relatively stable photocatalyst and can be prepared by gradually reducing $Bi^{3+}$ to $Bi^{2+}$ with the unsaturated carbon-carbon double bonds in oleate during hydrothermal process, which can be utilized to reduce $N_2$ to $NH_3$ under irradiation of light [22]. Besides, BiO also has the following advantages: (1) BiO is used as an n-type semiconductor with electrons as main charge carriers, and possesses suitable CB potential of approximately $-1.0$ eV; (2) the electronegativity of Bi (2.02) is greater than that of transition metals (Fe 1.83, Co 1.88, Ni 1.91, Cu 1.90), which is conducive to electron transfer between Bi and doping metal atom; (3) the radius of newly introduced atom should be small, which is conducive to the realization of doping, thus the cheap and easily available transition metals become the preferred choice. Furthermore, the transition metal Co can play the role of expedite the $CO_2$-adduct bonding [23], and it is reported that Co can play a prominent part in promoting charge transfer [24]. On the other hand, the doped Co can contribute to the valence band (VB) of metal oxides [25], which facilitates the upward shift of the VB and reduces the photocorrosion of catalyst itself. Given this, introducing Co atoms to regulate the microenvironment of low-valence Bi in BiO may be beneficial to promoting photogenerated electron transfer, improving the electron density of the active site and thus facilitating the activation of $CO_2$ molecules.

Inspired by the above, in the process of preparing BiO QDs, we added a small amount of transition metal Co for doping, and the photocatalyst containing Co single atoms was prepared. We found for the first time that Co single atoms act as the coordination atoms of second-shell to regulate the microenvironment of Bi active sites, thereby improving the efficiency of photogenerated charge separation and the electron density of Bi sites. It is corroborated that the Co single atoms can act as trap states to capture photogenerated charges and then transfer electrons to the Bi sites, thereby tailoring the electronic structure of Bi sites, and at the same time, improving the capacity of $CO_2$ adsorption and catalytic activity of $CO_2$ photoreduction. And the energy barrier needed to be crossed for the formation of key intermediate, *COOH, also largely decreases, thereby boosting the rate of $CO_2$ reduction.

## 2. Experimental

### 2.1. Catalyst synthesis

In a typical synthesis procedure, sodium oleate ($C_{17}H_{33}COONa$, 2.2

mmol) was added into 20 mL of deionized water, and then the mixture was stirred with ultrasonic to make it completely dissolved. The Bi $(NO_3)_3 \cdot 5$ H$_2$O (0.4 mmol) and a certain amount of Co(NO$_3$)$_2 \cdot 6$ H$_2$O (the molar ratio of Co to Bi is 0%, 0.5%, 1.0%, 2.0% and 3.0% respectively) were added into the above solution, which was stirred vigorously for 2 h. The obtained solution and another 20 mL of deionized water were transferred into 50 mL Teflon-sealed autoclave. After heating at 140 °C for 17 h, the autoclaves naturally cooled to room temperature, then the solids were collected by centrifugation and washed with ethanol for three times. Finally, after freeze-drying treatment, the obtained products are labeled as BiO QDs, Co/BiO(0.5%), Co/BiO(1.0%), Co/BiO(2.0%) and Co/BiO(3.0%), respectively.

### 2.2. Characterization

The crystalline phase and purity were detected by powder X-ray diffraction (XRD) with Cu-K$_\alpha$ radiation ($\lambda = 1.5418$ Å). The morphology and microstructure were characterized on transmission electron microscope (TEM, FEI Talos f20), and the high-resolution TEM (HRTEM) was taken on field emission TEM (FEI Tecnai G2 F20) with a spherical aberration corrector. Elemental analysis was obtained by using inductively coupled plasma–atomic emission spectrometry (ICP-AES, Varian 710-AES). X-ray photoelectron spectroscopy (XPS) was analyzed on a PHI 5300 ESCA with an Al K$_\alpha$ X-ray source. The Co K-edge and Bi L$_3$-edge X-ray absorption fine structure spectroscopy (XAFS) was measured at beamline BL14B2 of the Japanese Spring8 synchrotron radiation source. In situ diffuse reflectance infrared Fourier transform spectroscopy (DRIFTS) measurements were performed on a Nicolet iS50 FT-IR spectrometer (Thermo Scientific). The spectrometer was equipped with an in situ diffuse reflectance cell (Harrick). The $CO_2$ adsorption tests were carried out through ASAP2460 gas adsorption analyzer (Micromeritics Instrument Co.). Photoluminescence (PL) spectra were conducted on FLS-980 coupled with time-correlated single-photo-counting system. All electrochemical tests were conducted on CHI 760E electrochemical system with using a three-electrode system. The produced gas product was detected by gas chromatograph (FULI GC9790II) equipped with thermal-conductivity detector (TCD) and flame ionization detector (FID). The liquid phase product was analyzed by $^1$H nuclear magnetic resonance spectroscopy (NMR) on BrukerAvance 400 spectrometer. The product of $^{13}CO_2$ isotopic experiment was measured by gas chromatography-mass spectrometry (GC-MS, Agilent 7890A-5975 C).

### 2.3. Photocatalytic experiment

The reactions of photocatalytic $CO_2$ reduction were carried out by using a 55 mL of quartz tube sealed with plug. The photocatalyst (15 mg) and deionized water (10 mL) were continuously added into the quartz tube, which was treated with ultrasonic for 15 min. After the photocatalyst was uniformly dispersed in water, the high-purity $CO_2$ (99.999%) was bubbled into the mixture at a flow rate of 100 mL min$^{-1}$ for 30 min. Then the quartz tube was sealed with silicone plug and continued to use laboratory film to improve the gas tightness. The sealed quartz tube was placed on the magnetic stirrer, the light source was a 300 W xenon lamp with a cut-off filter of 420 nm, which was 10 cm away from the quartz tube. The 0.5 mL of gas was taken from the sealed quartz tube for testing and analysis after 4 h of irradiation.

### 2.4. Computational methods

We have employed the Vienna Ab Initio Package (VASP) to perform all the density functional theory (DFT) calculations within the generalized gradient approximation (GGA) using the Perdew-Burke-Ernzerhof (PBE) formulation [26–28]. We have chosen the projected augmented wave (PAW) potentials to describe the ionic cores and taken valence electrons into account using a plane wave basis set with a kinetic energy cutoff of 450 eV [29,30]. Partial occupancies of the Kohn-Sham orbitals

were allowed using the Gaussian smearing method and a width of 0.05 eV. The electronic energy was considered self-consistent when the energy change was smaller than $10^{-5}$ eV. A geometry optimization was considered convergent when the energy change was smaller than 0.05 eV $\text{Å}^{-1}$. Finally, the adsorption energies ($E_{ads}$) were calculated as $E_{ads} = E_{ad/sub} - E_{ad} - E_{sub}$, where $E_{ad/sub}$, $E_{ad}$, and $E_{sub}$ are the total energies of the optimized adsorbate/substrate system, the adsorbate in the structure, and the clean substrate, respectively. The free energy was calculated using the equation: $G = E_{ads} + ZPE - TS$, where G, $E_{ads}$, ZPE and TS are the free energy, total energy from DFT calculations, zero point energy and entropic contributions, respectively. The equilibrium lattice constants of BiO unit cell were optimized, when using a $10 \times 10 \times 10$ Monkhorst-Pack k-point grid for Brillouin zone sampling. And the (101) surface of BiO had been established with the lattice parameters a=b= 15.5341 Å, c= 22.344 Å, one Co atom was doped into the BiO surface. The vacuum spacing in a direction perpendicular to the plane of the structure is 18 Å for the surfaces. During structural optimizations, a $2 \times 2 \times 1$ k-point grid in the Brillouin zone was used for k-point sampling, and all atoms were allowed to relax.

## 3. Results and discussion

### 3.1. Structure analysis of Co doped BiO

The schematic illustration of material preparation is shown in Fig. S1, and the XRD patterns of BiO QDs with different Co doping amounts are depicted in Fig. 1a. The diffraction peaks of all samples can be indexed to rhombohedral BiO (JCPDS Card No. 27–0054), and no typical peaks of Co or Co oxides are detected, demonstrating the crystal structure of BiO QDs has not changed after introduction of Co. However, the diffraction peak of (101) plane is not sharp due to the small size of the QDs (Fig. S2) [22]. In the partial enlarged XRD patterns (Fig. S3), the diffraction peak of (110) plane gradually shifts to the large angle with the increase of Co doping amount, which may be caused by the substitution of Co atoms for Bi atoms. As the radius of Co atom is smaller than that of Bi, Co doping causes the lattice contraction, thus resulting in a positive shift [31]. From the TEM image in Fig. S4, pure BiO QDs show the spherical-like morphology with a mean diameter of $2 - 5$ nm, and the lattice fringes of 0.197 nm are ascribed to (104) plane. After doping with Co atoms, the resultant Co/BiO(1.0%) exhibits similar morphology and the single crystal nature (Fig. 1b). Concretely, the *d*-spacings of lattice fringes of 0.197 and 0.194 nm correspond to the (104) and (110) crystal plane of BiO, respectively. More than that, it distinctly illustrates that Co may exist in the form of alternative doping around Bi atoms. In Fig. S5, the dark spots (marked by orange circles) surrounded by bright spots (Bi atoms) can be classified as the light Co atoms rather than heavy Bi atoms in virtue of the Z-contrast difference [32]. And the integrated pixel intensity profiles along the white dashed rectangle in Fig. S5 were measured, which corroborates the conclusion that Co is atomically doped in the BiO lattice. Additionally, the content of doped Co was analyzed to be 0.91 mol% in total metal atoms by ICP-AES in Table S1, which is close to the theoretical content.

In order to investigate the influence of Co doping on the chemical states in BiO, XPS measurement was performed with Ar etching treatment and the results are shown in Fig. 1c. The binding energies of Bi 4 $f_{5/2}$ and Bi 4 $f_{7/2}$ peaks of original BiO are located at 162.5 and 157.3 eV [33], while the corresponding peaks of Co/BiO(1.0%) shift to low binding energy. This phenomenon may be attributed to the fact that the doped Co transfers partial electron to Bi, thus causing the negative shift of Bi 4 f peaks. Similarly, the O 1 s spectrum of Co/BiO(1.0%) is situated at 531.1 eV (Fig. S6), obviously lower than that of BiO. In addition, a conspicuous peak at 795.1 eV assigned to Co cation is observed in Co 2p spectrum of Co/BiO(1.0%), further manifesting the Co atoms enter into the crystal phase of BiO.

To further probe the electronic structure and coordination environment of Co atoms at atomic level, X-ray absorption fine structure (XAFS) measurements were conducted. As displayed in Fig. 1d, the normalized X-ray absorption near edge structure (XANES) curve of Co K-edge for Co/BiO(1.0%) is significantly distinguishable from the references of Co foil and CoO, while Co/BiO(1.0%) displays relatively smooth XANES profile. The absorption edge position of Co/BiO(1.0%) is located between those of Co foil and CoO, which indicates the Co single atoms possess special electronic structure with positive charges in the valence state between 0 and + 2. It is consistent with the analysis result of XPS. The Fourier-transformed extended X-ray absorption fine structure (FT-EXAFS) curve of Co/BiO(1.0%) in Fig. 1e just reveals one main peak located at 1.60 Å, which can be classified as Co-O coordination shell. In contrast, the main peak of Co foil can be detected at 2.18 Å, corresponding to the metallic Co-Co coordination. This result demonstrates that the doped Co atoms in Co/BiO(1.0%) are atomically dispersed. Moreover, the wavelet transform (WT) of Co K-edge EXAFS oscillations (Fig. 1f) also certify the atomic dispersion of Co in Co/BiO(1.0%). In addition, the Co K-edge spectra in $k^3$-weighted EXAFS are presented in Fig. 1g to explore the coordination configuration of Co atom. The curve obtained from Co/BiO(1.0%) at k space is obviously different from those of Co foil and CoO, which can safely exclude the possibility of containing Co nanoparticles or clusters but confirm the presence of atomically dispersed Co. The shift of peaks in Co/BiO(1.0%) is not only related to the coordination number of O, but also affected by the Bi atoms at the secondary coordination shell. EXAFS fitting analysis was conducted to extract the structural parameters as well as acquire the quantitative coordination configuration of Co atoms. As shown in Fig. 1h, the fitting result of R space reveals that a main peak is originating from Co-O bond and the first-shell of Co atom display the coordination number of 3.9 (nearly 4.0), and the average bond length of Co-O in Co/BiO(1.0%) is 2.02 Å (Table S2). Thus, the local coordination structure of Co single atom can be inferred as shown by the inset in Fig. 1h.

As presented in Fig. 1i, the slight difference in intensity as well as position of the peaks corresponding to $L_3$-edge absorption edge at approximately 13438 eV suggest that the Bi atoms in Co/BiO(1.0%) are of diverse environments due to Co incorporation [34]. The slight decrease of peak intensity (inset of Fig. 1i) implies that the valence state of Bi in Co/BiO(1.0%) is slightly lower than + 2, suggesting Bi atoms have received some electrons. The FT curve of EXAFS for Co/BiO(1.0%) (Fig. 1j) exhibits only one dominant peak around 1.68 Å, which is close to the curve detected in BiO QDs, clearly indicating almost the same coordination environment around Bi in both Co/BiO(1.0%) and BiO QDs. The $k^3$-weighted Bi $L_3$-edge EXAFS spectra of Co/BiO(1.0%) and BiO QDs are also similar in curve type and strength (Fig. S7), manifesting that first-shell coordination atoms of Bi has not changed. What's more, compared with the WT contour plots of BiO QDs and Bi foil, there is a strong WT signal at 3.7 $\text{Å}^{-1}$ derived from the Bi-O contribution (Fig. S8), which further confirms the first-shell coordination atoms of Bi are all O atoms. The fitting curve of R space (Fig. 1k) discloses that Bi atoms are coordinated with four O atoms and the mean bonding length is 2.25 Å (Table S3). Based on the above analysis of characterizations, the local atomic structure model of Co/BiO(1.0%) can be confirmed as illustrated by the inset in Fig. 1k. As can be seen, one Bi atom directly coordinates with four O atoms, while the doped Co atom instead of Bi atom coordinates with O atom in the secondary coordination environment.

### 3.2. Influence of Co single atom on charge separation and transfer

To explore the migration direction of photogenerated electrons, the work function ($\Phi$) is taken into account [35]. Based on the first-principles results, the calculated work functions of BiO QDs and Co/BiO(1.0%) are 5.40 and 5.33 eV (Fig. 2a, b) respectively, suggesting the work function is reduced after Co doping. A small value of work function coupled with weaker electron binding restriction ability can effectively accelerate the photo-induced electron transfer [36]. However, excessive doping will lead to the formation of too many trapping
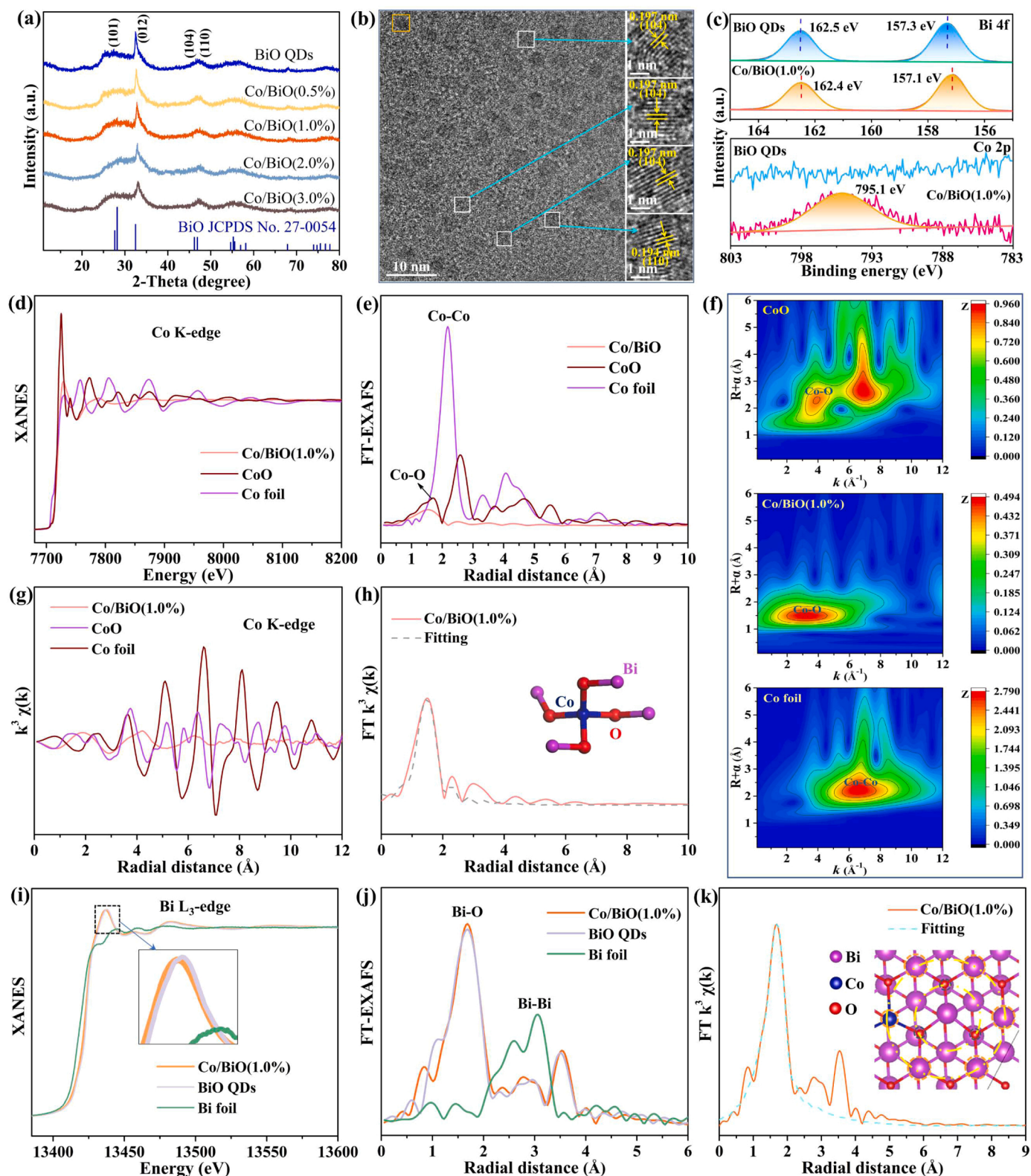
**Fig. 1.** (a) XRD patterns of BiO and Co/BiO QDs. (b) TEM image of Co/BiO(1.0%). (c) High-resolution XPS spectra of Bi 4 f and Co 2p. (d) XANES spectra at the Co K-edge of Co/BiO(1.0%), Co foil and CoO. (e) Fourier transform at the Co K-edge of Co/BiO(1.0%), Co foil and CoO. (f) WT of CoO, Co/BiO(1.0%) and Co foil, respectively. (g) k space EXAFS spectra of Co/BiO(1.0%), Co foil and CoO at the Co K-edge. (h) Corresponding EXAFS fitting curves of Co/BiO(1.0%) at R space. (i) XANES spectra at the Bi $L_3$-edge of Co/BiO(1.0%), Bi foil and BiO QDs. (j) Fourier transform at the Bi $L_3$-edge of Co/BiO(1.0%), Bi foil and BiO QDs. (k) Corresponding EXAFS fitting curves of Co/BiO(1.0%) at R space.
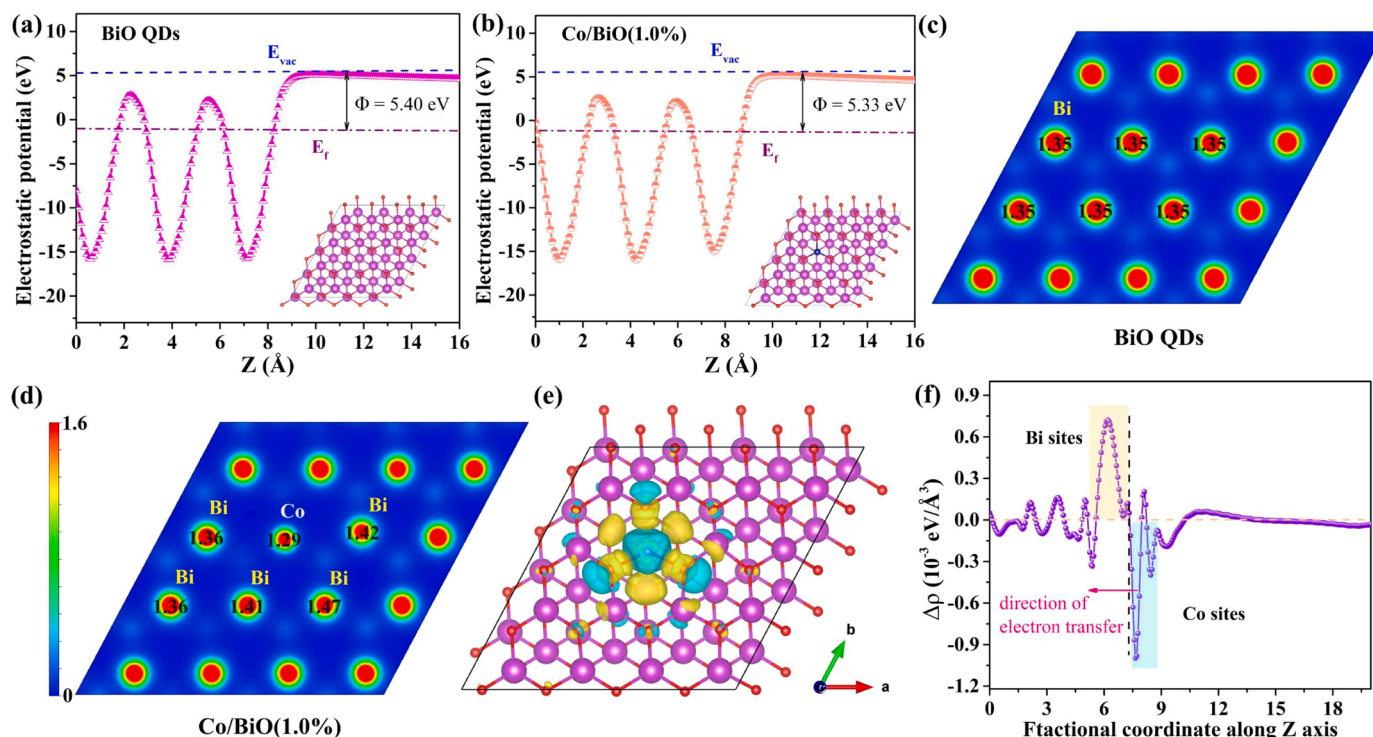
**Fig. 2.** Calculated electrostatic potentials of (a) BiO QDs and (b) Co/BiO(1.0%). The Bader charge values of different atoms in (c) BiO QDs and (d) Co/BiO(1.0%). (e) Difference charge density map of Co/BiO(1.0%), isosurface value is set to be 0.003 eV $\text{Å}^{-3}$. (f) Corresponding planar-averaged electron density difference.

centers in the bulk of photocatalyst, which restrains the separation and migration of photogenerated charges. To clarify the promotion effect of Co single atom on electron transfer, the Bader charge distributions of pure BiO QDs and Co/BiO(1.0%) were analyzed by way of DFT calculations. As displayed in Fig. 2c, the Bi sites in BiO QDs possess identical Bader charge (1.35). However, the introduction of Co induces a significant increase of charge amount for Bi sites around the Co single atom in Co/BiO(1.0%), increasing the Bader charge from 1.35 up to the highest 1.47 (Fig. 2d). In the meantime, the Bader charge of Co atomic site is the lowest (1.29), intimating that the electrons can transfer from Co single atom to the neighboring Bi atoms [37], in agreement with the above analysis results of XPS and XAFS. Furthermore, the differential charge density diagram of Co/BiO(1.0%) is shown in Fig. 2e, the electron accumulation and depletion in the space are marked as yellow and blue clouds respectively. Thereinto, the electron accumulation on Bi atoms and depletion on Co single atom provide intuitive evidence of electron transfer. Fig. 2f plots the corresponding planar-averaged electron density difference, and the positive as well as negative values stand for electron accumulation and depletion, respectively [38]. Apparently, Bi sites gain electrons while Co sites lose electrons, confirming the fact that electron transfer from Co single atoms to Bi atoms, which endows Bi sites with high electron density. In addition, in situ XPS results under light and dark conditions are shown in Fig. S9. Under the condition of photoexcitation, the fitting peaks of Bi 4 f shift to the direction of low binding energy (Fig. S9a), while the peak of Co single atoms shifts to the direction of high binding energy (Fig. S9b), which indicates that Co single atoms as the trap states can transfer the captured photogenerated electrons to the Bi active sites. O atoms as the first-shell coordination atoms also get some photogenerated electrons, which cause them to move towards the direction of low binding energy (Fig. S9c). The analysis results of in situ XPS are consistent with the XAFS, work function, Bader charge and differential charge density analysis results, further indicating that electrons are transferred from the Co single atoms to the Bi active sites.

The separation efficiency of photogenerated carriers is very

important for investigating the catalytic efficiency, which influences the overall reaction rate. In consideration of this, steady-state PL tests were conducted at an excitation wavelength of 380 nm. As displayed in Fig. 3a, compared with the high intensity of pure BiO QDs, the fluorescence intensities of Co doped BiO are significantly reduced. Among them, Co/BiO(1.0%) shows the weakest intensity, indicating that this doping concentration can effectively inhibit the recombination of photogenerated carriers [39]. Furthermore, the photocurrent densities of Co/BiO materials are also significantly improved, wherein Co/BiO(1.0%) has the highest photocurrent density, which is 10 times higher than that of pure BiO QDs. Similarly, the results of electrochemical impedance spectroscopy (EIS) further illustrate that the existence of Co single atoms can reduce the transfer resistance of photogenerated carriers as well as promote more electrons to migrate to the surface for participating in $CO_2$ reduction reaction (Fig. S10).

The time-resolved PL decay curves were measured with incident laser wavelength of 380 nm and obtained emission peaks were located at 460 nm. The acquired fluorescence lifetime decay curves are depicted in Fig. 3c, and the biexponential fitting results are 0.89 and 1.36 ns for BiO QDs and Co/BiO(1.0%) respectively. Through further analysis, the isolated Co single atoms have little impact on $\tau_1$, but endow 47% increase for $\tau_2$. The two relaxation processes can be explained by that the fast decay component of $\tau_1$ (~0.3 ns) is accounted for trapping of electrons from CB into trap states within the bandgap, while the slower decay component of $\tau_2$ denotes the recombination of captured electrons and VB holes [40]. Accordingly, the Co single atoms at the secondary coordination shell may serve as the trap states to capture photogenerated electrons, thus more long-lived electrons promote the separation of electron-hole pairs, which provides increased opportunities for taking part in the $CO_2$ reduction reaction [41]. Moreover, the surface photovoltage (SPV) curves (Fig. S11) exhibit the intensity of Co/BiO(1.0%) is much higher than that of BiO QDs, confirming the strong thermodynamic driving force for the separation of photogenerated carriers. Based on ultraviolet-visible diffuse reflectance spectra (Fig. S12a), the bandgaps can be determined by using the
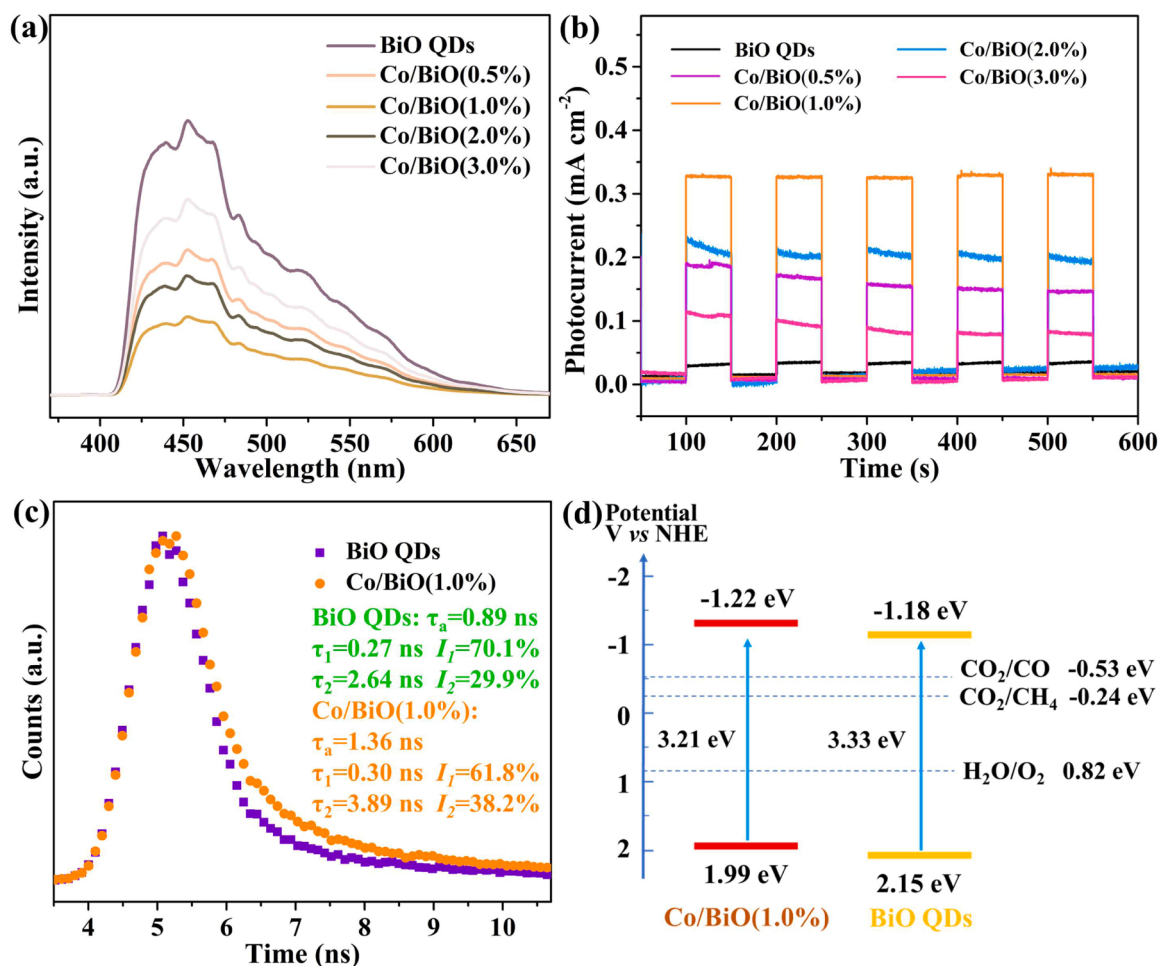
**Fig. 3.** (a) Steady-state PL spectra. (b) Transient photocurrent response. (c) Time-resolved PL spectra of photocatalytic $CO_2$ reduction systems with BiO QDs and Co/BiO(1.0%). (d) Band structure alignments of BiO QDs and Co/BiO(1.0%).

Tauc/Davis-Mott model (Fig. S12b) [42]. And the values of VB were measured by XPS valence spectra (Fig. S12c), the final results of energy band are shown in Fig. 3d. The upward shift of the CB represents an improvement in the photocatalytic reduction ability of the catalyst [43, 44]. And the upward shift of the VB indicates that the oxidation ability of BiO decreases after Co doping, and thus the photocorrosion ability of Co/BiO(1.0%) decreases, which is beneficial for improving the stability of photocatalysts. Additionally, the flat band potentials ($E_{fb}$) were calculated from the Mott-Schottky curves (Fig. S13), which are − 0.75 V and − 0.87 V (vs NHE) for BiO and Co/BiO(1.0%) respectively. It suggests that the electrons are more likely to overflow from bulk phase to surface active sites [45], and ultimately improving photocatalytic $CO_2$ reduction performance.

### 3.3. Photocatalytic performance of $CO_2$ reduction

In an effort to validate the positive effect of regulating the coordination environment of Bi sites on photocatalytic reduction of $CO_2$, a series of experiments based on BiO and Co/BiO catalysts were carried out. As shown in Fig. 4a, pure BiO QDs disclose low photocatalytic activity, and the evolution rate of CO product is 14 μmol $g^{-1}$ in 4 h. After introducing Co, the photocatalytic performance of BiO firstly increases and then decreases along with the enhance of Co content. As expected, Co/BiO(1.0%) reveals the highest photocatalytic activity for $CO_2$ reduction, the CO yield reaches 78 μmol $g^{-1}$ after 4 h of irradiation, which is about 5.6 times that of pure BiO QDs. And no water reduction product ($H_2$) or liquid products like HCHO, $CH_3OH$, HCOOH and

$C_2H_5OH$ were detected in the reaction process (Fig. S14). According to the above analysis, the Co single atom in the lattice of BiO acts as trap state to depress the recombination of photogenerated carriers, and improves the electron migration rate and the electron density on Bi site, thereby promoting the improvement of photocatalytic performance [46]. Additionally, to exclude the effect of vacancies, the electron spin resonance (EPR) tests were performed on BiO QDs and Co/BiO(1.0%). As shown in Fig. S15, no obvious EPR signal peak was detected in BiO as well as Co/BiO(1.0%), indicating that the improvement of photocatalytic activity is independent of defect. Moreover, the comparison of photocatalytic performance with other metal-doped BiO is shown in Fig. S16. The results indicate that the photocatalytic performance of BiO can be limitedly promoted by doping Fe, Ni and Cu, but largely improved by Co doping. Additionally, in order to investigate the effect of directly regulating the coordination environment of Bi sites on catalytic $CO_2$ reduction, non-metal doped BiO materials were prepared. The chemicals of urea, $NaH_2PO_2 \cdot H_2O$ and thioacetamide were used as N, P and S sources for preparation of N/BiO, P/BiO and S/BiO, respectively. And their coordination is generally located in the first coordination shell of the metal [47,48]. The mass ratio of BiO QDs to chemicals was 1:5, and after grinding, the mixture was calcined at 200 °C under Ar atmosphere for 1 h. The XRD patterns of the prepared non-metal doped BiO (Fig. S17a) show that the positions and shapes of all diffraction peaks are consistent with those of pure BiO, indicating that non-metal doping does not cause the destruction of BiO crystal phase. The comparison of photocatalytic $CO_2$ reduction performance is shown in Fig. S17b. It is worth noting that the photocatalytic performance of non-metal doped BiO
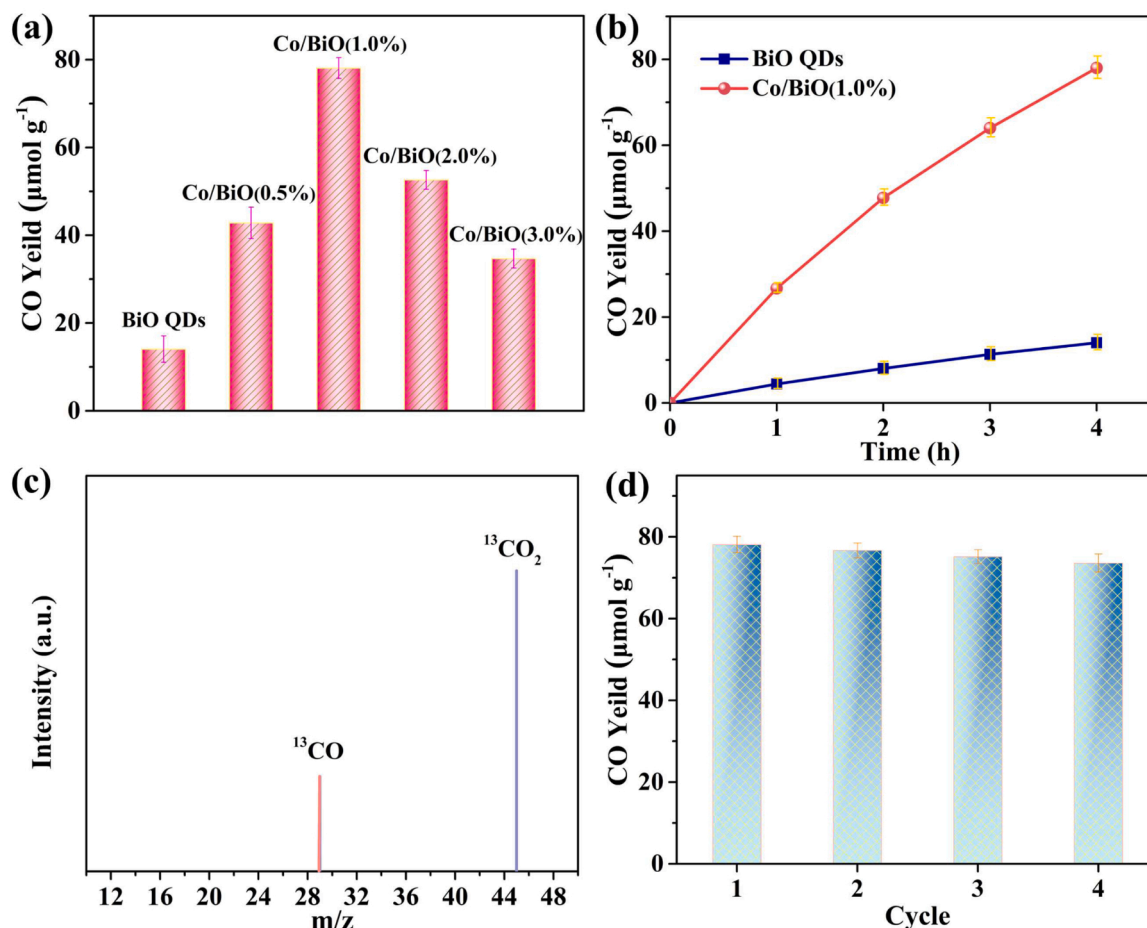
**Fig. 4.** (a) Effect of Co doping amount on catalytic activity. (b) The evolution rate of CO as a function of irradiation time. (c) The mass spectrum analysis of product over Co/BiO(1.0%) with $^{13}CO_2$ as feedstock. (d) Recycle tests of Co/BiO(1.0%).

decreases instead of increasing, which demonstrates that directly regulating the coordination environment of Bi site is unfavorable for improving catalytic activity. Therefore, regulating the secondary coordination environment of BiO is more advantageous for improving the photocatalytic $CO_2$ reduction performance.

Fig. 4b exhibits the time-related accumulation of CO, which increases with the exposure time of light. It verifies the intrinsic mechanism as photocatalytic reaction. Furthermore, compared experiments were carried out with the shortage of photons, catalysts, $CO_2$ and $H_2O$, respectively, and the results implied that no carbon-containing products were formed (Fig. S18). The isotope labeling experiment was performed through utilizing $^{13}CO_2$ instead of $CO_2$ to further determine the origin of carbon. The result shown in Fig. 4c ascertains that the released CO stemmed from $CO_2$ reduction. Apart from the improvement of catalytic activity, Co/BiO(1.0%) also exhibits good stability after four consecutive photocatalytic cycles (Fig. 4d). The cyclic experimental results show that the catalytic efficiency of BiO QDs decreased by 29.4% after four cycles (Fig. S19), while Co/BiO(1.0%) only decreased by 5.8%. The decrease in the catalytic efficiency is due to the occurrence of photocorrosion on photocatalyst. Obviously, introducing Co single atoms into BiO QDs can significantly suppress the photocorrosion and improve photocatalytic stability. Furthermore, the XRD, TEM and XPS analysis of recycled Co/BiO(1.0%) display no noticeable changes of structure and morphology with the fresh one (Fig. S20 and S21), further verifying the favorable durability of BiO QDs after the introduction of Co single atoms. Additionally, the oxidation half-reaction was also studied, the experimentally measured $H_2O_2$ is very close to the theoretical value (Fig. S22), which suggests that the photocatalytic oxidation half-

reaction is to oxidize water into $H_2O_2$ [49,50].

### 3.4. Study on $CO_2$ adsorption and catalytic mechanism

The adsorption of reactants is generally regarded as a prerequisite for photocatalytic reaction [51]. In view of this, the $CO_2$ adsorption measurement was performed to detect the adsorption behavior on the surface of photocatalysts. As illustrated in Fig. 5a, Co/BiO(1.0%) adsorbs around 1.6 times as much $CO_2$ as BiO QDs, implying that Co/BiO(1.0%) containing Co single atoms possesses higher $CO_2$ affinity than BiO QDs. Moreover, the band center energies ($\varepsilon_{p,Bi}$) of BiO QDs and Co/BiO(1.0%) were also investigated to elucidate the adsorption capacity. As displayed in Fig. 5b, the $\varepsilon_{p,Bi}$ (−2.081) of Co/BiO(1.0%) moves further towards the $E_f$ (Fermi level) than that of BiO QDs ($\varepsilon_{p,Bi} = -2.736$). Based on the theory of Nørskov, the closer the value of $\varepsilon_{p,Bi}$ is to the $E_f$, the more negative the adsorption energy of the reactant molecule is on Bi site [52]. Moreover, the crystal orbital Hamiltonian population (COHP) curves as well as integrated COHP values (ICOHP) of $CO_2$ adsorbed on Bi sites were also calculated. As presented in Fig. 5c, the value of −ICOHP (2.550 eV) for Co/BiO(1.0%) is obviously higher than that for BiO QDs (1.920 eV). Notably, the more negative ICOHP value suggests the stronger interaction of metal-$CO_2$ [53]. This calculation result is mutually confirmed by the result of $CO_2$ adsorption experiment, and existence of Co single atoms endows the Co/BiO(1.0%) with strong $CO_2$ adsorption capacity. In addition, the in situ DRIFTS spectra of Co/BiO(1.0%) (Fig. 5d) show a broad absorption peak centered at 2345 cm$^{-1}$ and the absorption peak intensity increases with the extension of the illumination time [54,55]. However, for BiO QDs, the absorption peak at the
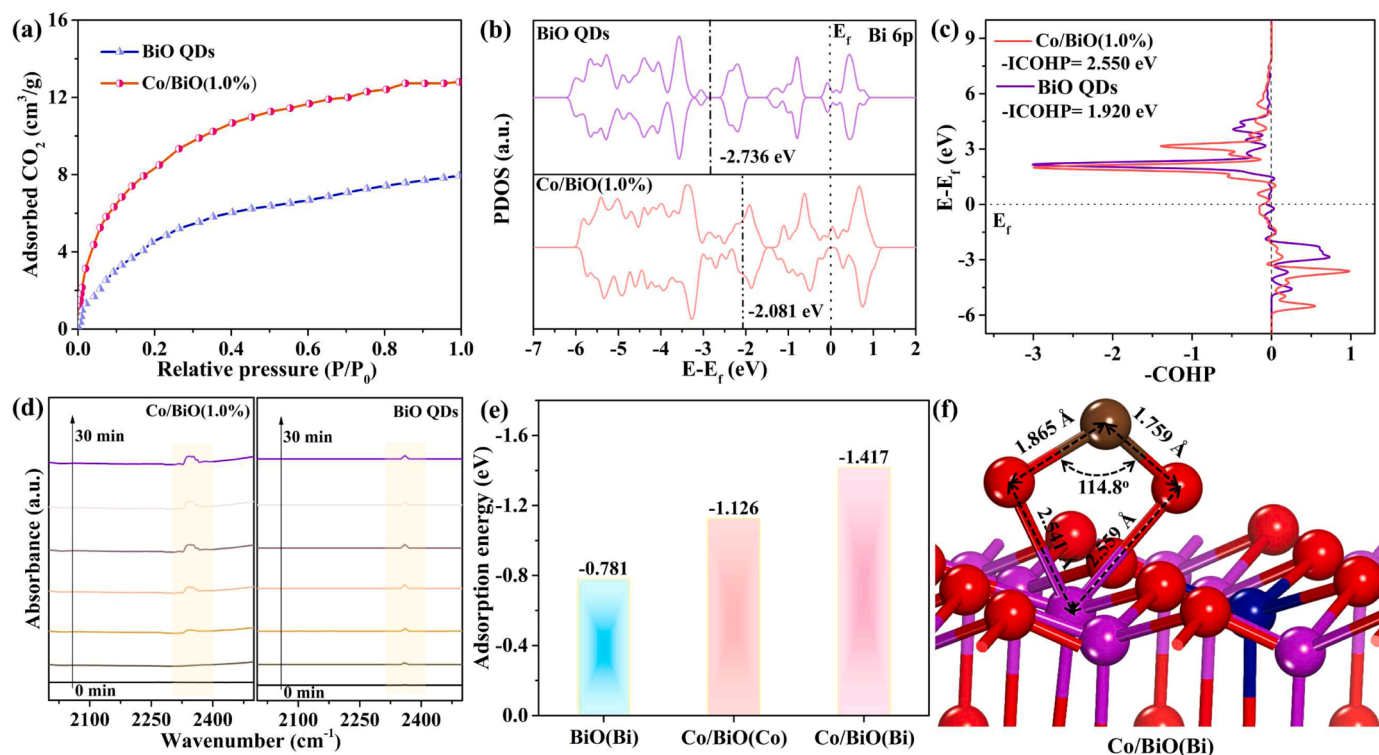
**Fig. 5.** (a) The adsorption curves of $CO_2$ with BiO QDs and Co/BiO(1.0%). (b) The partial density of states with the band center energy marked for Bi 6p of BiO QDs and Co/BiO(1.0%). (c) COHP analysis for metal-O band towards adsorption of $CO_2$ on BiO QDs and Co/BiO(1.0%), including their respective ICOHP values. (d) *In situ* DRIFTS spectra of the $CO_2$ adsorption over BiO QDs and Co/BiO(1.0%). (e) Adsorption energies of $CO_2$ at different sites. (f) The adsorption structures, bond lengths and bond angle of $CO_2$ adsorbed at Bi site of Co/BiO(1.0%).
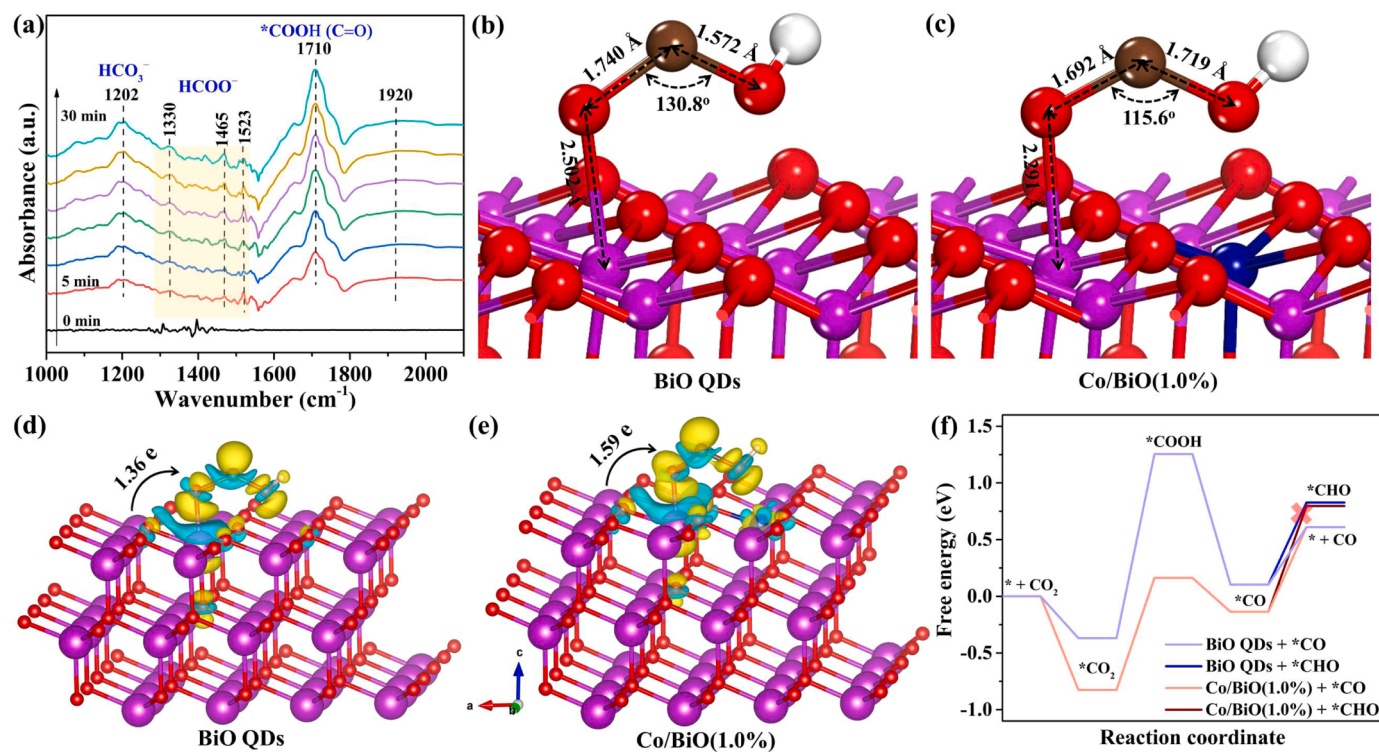


**Fig. 6.** (a) *In situ* DRIFTS spectra obtained at different irradiation times during $CO_2$ photoreduction on Co/BiO(1.0%). Spatial configurations of intermediate *COOH on (b) BiO QDs and (c) Co/BiO(1.0%). Charge difference density of *COOH on (d) BiO QDs and (e) Co/BiO(1.0%), isosurface set at 0.005e $Å^{-3}$. (f) Calculated free energy diagrams for $CO_2$ reduction into CO on BiO QDs and Co/BiO(1.0%).

same position becomes narrow and sharp, proving BiO QDs has weak adsorption capacity for $CO_2$. On the other side, the CB in BiO is mainly composed of Bi 6p [44], when the Co single atoms are introduced into BiO, the Co 3d orbital participates in the CB composition, which causes the CB of Co/BiO(1.0%) to move upwards. The hybridization and redistribution of Co and Bi atomic orbitals improve the interaction with the C 2p orbital in $CO_2$, thereby improving the $CO_2$ adsorption capacity [56,57].

For the sake of obtaining information about catalytic sites at an atomic level, the adsorption energies of $CO_2$ over different adsorption sites are calculated and shown in Fig. 5e. The adsorption energy at Bi site of Co/BiO(1.0%) (marked as Co/BiO(Bi)) is − 1.417 eV, apparently lower than that at Co site (−1.126 eV), whereas the adsorption energy of $CO_2$ molecule at Bi site (BiO(Bi)) is the highest (−0.781 eV). As opposed to free $CO_2$ with a O−C−O bond angle of 180° and a C−O bond length of 1.18 Å [7], the $CO_2$ molecule adsorbed at Bi site of Co/BiO(1.0%) is chemically activated, leading to the bond angle of O−C−O bending (114.8°) and both bonds of C−O elongating (1.865 and 1.759 Å) (Fig. 5f). Moreover, due to the existence of Co single atom in the secondary coordination environment, the activation parameters of $CO_2$ at Bi site of Co/BiO(1.0%) are superior to those at the Co site of Co/BiO (1.0%) and Bi site of BiO (Fig. S23). Consequently, Bi is determined as the active site in Co/BiO(1.0%) for adsorption and activation of $CO_2$ molecules. From the above analysis, Co single atoms are conducive to capturing photogenerated charges for improving the separation efficiency, while the electrons tend to transfer from Co single atoms to Bi active sites, which increases the electron density of neighboring Bi sites, hence largely promoting the $CO_2$ photoreduction rate.

In order to gain deep insights into the photoconversion mechanism, the $CO_2$ reduction intermediates were investigated by in situ DRIFTS. As shown in Fig. 6a, the distinct peak located at 1202 $cm^{-1}$ is ascribed to bicarbonate ($HCO_3^-$) and gradually increases with irradiation time on Co/BiO(1.0%) [56], suggesting that the adsorbed $CO_2$ molecules can be continuously transformed into carbon-containing active species. The obtained infrared absorption peaks in the range of 1330 − 1550 $cm^{-1}$ are classified as $HCOO^-$ species, the peak at 1330 $cm^{-1}$ is attributed to the stretching vibration of C−O in the formate [57], and the peaks located at 1465 and 1523 $cm^{-1}$ assigned to hydrocarboxyl group start to appear and accumulate as the exposure time increases. More importantly, the vital intermediate of *COOH was identified as the strongest absorption peak, which is situated at 1710 $cm^{-1}$ (C=O bending vibration) [58]. Besides, the broad peak centered at 1920 $cm^{-1}$ is attributed to the bridge-bonded CO on Bi atoms [57], so it can be inferred that intermediate *COOH will be converted to CO after further hydrogenation. Fig. 6b and c demonstrate the optimized geometry structures of *COOH at Bi sites of BiO QDs and Co/BiO(1.0%) respectively. For BiO QDs, the angle of O−C−O in intermediate *COOH is 130.8° with the bond length of C−OH being 1.572 Å. Nevertheless, the Co single atom can provide electrons to Bi sites, which promotes the increase of electron density at Bi sites. As a result, the angle of O−C−O on Bi site of Co/BiO (1.0%) reduces to 115.6° and the bond length of C−OH increases to 1.719 Å, which is in favor for further hydrogenation and dehydration to form CO product.

For the purpose of intuitive display of getting or losing electrons in the production process of intermediate *COOH, the distributions of differential charge density of BiO QDs and Co/BiO(1.0%) were explored and shown in Fig. 6d and e, respectively. Contrary to BiO QDs, the electron transfer from the Co/BiO(1.0%) surface to *COOH is markedly improved. Specifically, the total charge (Δq) of *COOH is increased from 1.36 e in BiO QDs to 1.59 e in Co/BiO(1.0%). This is because the electrons could transfer from Co single atom in the second-shell to the central Bi site, thereby boosting its electron density. And as a consequence, the electron-enriched Bi site in Co/BiO(1.0%) possesses stronger bonding ability with O in *COOH (2.291 Å) than that in BiO QDs (2.502 Å), which is propitious to stabilize the *COOH and thus promote the reduction of $CO_2$. To further unravel the secret of the activity

improvement, the possible reaction paths were studied by means of free energy calculations, the corresponding intermediate configurations are illustrated in Fig. S24. The formation of *COOH on BiO QDs needs 1.25 eV of energy expenditure, much higher than the energy expenditure of *COOH formation (0.16 eV) on Co/BiO(1.0%) (Fig. 6f). Then the electrons continue to transfer to the intermediate *COOH, causing the C-O bond to break, thus forming CO product. On the contrary, the further hydrogenation of intermediate *CO into *CHO requires crossing very high energy barriers, which is a difficult pathway over BiO or Co/BiO photocatalysts to produce $CH_4$ [59]. On the other hand, the Co single atoms in the secondary coordination environment affect the photocatalytic performance by regulating electron transfer and $CO_2$ adsorption. And the elementary reaction steps of $CO_2$ molecules on active site Bi have not changed before and after Co doping (Fig. 6f), so the product is still CO.

## 4. Conclusion

In summary, BiO QDs containing Co single atoms were inadvertently obtained by a simple one-step hydrothermal reaction. The HRTEM and XAFS results prove that the doped Co exists in the form of single atoms in the secondary coordination environment of Bi sites. Significantly, the photogenerated electrons could transfer from Co single atom to neighbouring Bi atom, endowing Co/BiO(1.0%) with fast electron transfer rate, good charge separation efficiency, and high electron density. Notably, Bi atom in Co/BiO(1.0%) is determined as active site, which also possesses much higher adsorption and activation capacity of $CO_2$ molecules than that in pure BiO QDs. As a result, Co/BiO(1.0%) shows a superior photocatalytic efficiency for $CO_2$ reduction, and the CO yield is 5.6 times that of pure BiO QDs. DFT calculations further indicate that the $CO_2$ molecules is more feasible to be activated on Bi sites of Co/BiO (1.0%) than BiO QDs, due to the enhanced electron density acquired from Co single atoms. But beyond that, the energy barrier needed to be crossed for the formation of *COOH is smaller on Co/BiO(1.0%) than that on BiO QDs, validating the promotion effect of Co single atom. This work opens up new ideas for the regulation of coordination environment and the application of single atoms, and also provides a new insight for photocatalytic $CO_2$ reduction.

## CRediT authorship contribution statement

**Yong Xu:** Investigation, Methodology, Data curation, Conceptualization, Writing – original draft, Review & editing. **Man Zhang:** Data curation, Investigation, Review & editing. **Jianfei Long:** Review & editing. **Weili Dai:** Funding acquisition, Writing – review & editing, Supervision. **Ping Wang:** Review & editing. **Lixia Yang:** Review & editing. **Jianping Zou:** Review & editing. **Xubiao Luo:** Funding acquisition, Supervision.

## Declaration of Competing Interest

The authors declare that they have no known competing financial interests or personal relationships that could have appeared to influence the work reported in this paper.

## Data availability

Data will be made available on request.

## Acknowledgements

## Appendix A. Supporting information

Supplementary data associated with this article can be found in the online version at doi:10.1016/j.apcatb.2023.123230.

## References

[1] Q. Yi, W. Li, J. Feng, K. Xie, Carbon cycle in advanced coal chemical engineering, Chem. Soc. Rev. 44 (2015) 5409–5445.

[2] J. Artz, T.E. Müller, K. Thenert, J. Kleinekorte, R. Meys, A. Sternberg, A. Bardow, W. Leitner, Sustainable conversion of carbon dioxide: an integrated review of catalysis and life cycle assessment, Chem. Rev. 118 (2018) 434–504.

[3] F. Zeng, C. Mebrahtu, X. Xi, L. Liao, J. Ren, J. Xi, H. Heeres, R. Palkovits, Catalysts design for higher alcohols synthesis by $CO_2$ hydrogenation: trends and future perspectives, Appl. Catal. B: Environ. 291 (2021), 120073.

[4] J. Albero, Y. Peng, H. García, Photocatalytic $CO_2$ reduction to C2+ products, ACS Catal. 10 (2020) 5734–5749.

[5] F. Wang, R. Fang, X. Zhao, X. Kong, T. Hou, K. Shen, Y. Li, Ultrathin nanosheet assembled multishelled superstructures for photocatalytic $CO_2$ reduction, ACS Nano 16 (2022) 4517–4527.

[6] Y. He, C. Chen, Y. Liu, Y. Yang, C. Li, Z. Shi, Y. Han, S. Feng, Quantitative evaluation of carrier dynamics in full-spectrum responsive metallic $ZnIn_2S_4$ with indium vacancies for boosting photocatalytic $CO_2$ reduction, Nano Lett. 22 (2022) 4970–4978.

[7] Y. Xu, J. Mo, J. Long, L. Tu, W. Dai, L. Yang, S. Luo, $Co_2P$ nanorods with exposure of high-index facets for efficient photochemical reduction of $CO_2$ by promoting the directional transfer of electrons, J. Energy Chem. 73 (2022) 322–329.

[8] S. Liu, L. Chen, T. Liu, S. Cai, S. Cai, X. Zou, J. Jiang, Z. Mei, Rich S vacant g-$C_3N_4$@ $CuIn_5S_8$ hollow heterojunction for highly efficient selective photocatalytic $CO_2$ reduction, Chem. Eng. J. 424 (2021) 130325.

[9] J. Li, W. Pan, Q. Liu, Z. Chen, Z. Chen, X. Feng, H. Chen, Interfacial engineering of $Bi_{19}Br_3S_{27}$ nanowires promotes metallic photocatalytic $CO_2$ reduction activity under near-infrared light irradiation, J. Am. Chem. Soc. 143 (2021) 6551–6559.

[10] L. Liu, H. Huang, Z. Chen, H. Yu, K. Wang, J. Huang, H. Yu, Y. Zhang, Synergistic polarization engineering on bulk and surface for boosting $CO_2$ photoreduction, Angew. Chem. Int. Ed. 33 (2021) 18303–18308.

[11] L. Ling, L. Jiao, X. Liu, Y. Dong, W. Yang, H. Zhang, B. Ye, J. Chen, H. Jiang, Potassium-assisted fabrication of intrinsic defects in porous carbons for electrocatalytic $CO_2$ reduction, Adv. Mater. 34 (2022), 2205933.

[12] D. Tantraviwat, A. Nattestad, J. Chen, B. Inceesungvorn, Enhanced photoactivity and selectivity over BiOI-decorated $Bi_2WO_6$ microflower for selective oxidation of benzylamine: role, BiOI Mech., J. Colloid Interf. Sci. 629 (2023) 854–863.

[13] Y. Cao, L. Guo, M. Dan, D. Doronkin, C. Han, Z. Rao, Y. Liu, J. Meng, Z. Huang, K. Zheng, P. Chen, F. Dong, Y. Zhou, Modulating electron density of vacancy site by single Au atom for effective $CO_2$ photoreduction, Nat. Commun. 12 (2021) 1675.

[14] Q. Chen, W. Mo, G. Yang, S. Zhong, H. Lin, J. Chen, S. Bai, Significantly enhanced photocatalytic $CO_2$ reduction by surface amorphization of cocatalysts, Small 17 (2021), 2102105.

[15] Y. Liu, J. Sun, H. Huang, L. Bai, X. Zhao, B. Qu, L. Xiong, F. Bai, J. Tang, L. Jing, Improving $CO_2$ photoconversion with ionic liquid and Co single atoms, Nat. Commun. 14 (2023) 1457.

[16] G. Wang, Z. Chen, T. Wang, D. Wang, J. Mao, P and Cu dual sites on graphitic carbon nitride for photocatalytic $CO_2$ reduction to hydrocarbon fuels with high $C_2H_6$, Evol., Angew. Chem. Int. Ed. 61 (2022), e202210789.

[17] Y. Bo, C. Gao, Y. Xiong, Recent advances in engineering active sites for photocatalytic $CO_2$ reduction, Nanoscale 12 (2020) 12196–12209.

[18] X. Wang, Z. Chen, X. Zhao, T. Yao, W. Chen, R. You, C. Zhao, G. Wu, J. Wang, W. Huang, J. Yang, X. Hong, S. Wei, Y. Wu, Y. Li, Regulation of coordination number over single Co sites: triggering the efficient electroreduction of $CO_2$, Angew. Chem. Int. Ed. 57 (2018) 1944–1948.

[19] J. Qin, H. Liu, P. Zou, R. Zhang, C. Wang, H. Xin, Altering ligand fields in single-atom through second-shell anion modulation boosts the oxygen reduction reaction, J. Am. Chem. Soc. 144 (2022) 2197–2207.

[20] L. Cheng, X. Yue, L. Wang, D. Zhang, P. Zhang, J. Fan, Q. Xiang, Dual-single-atom tailoring with bifunctional integration for high-performance $CO_2$ photoreduction, Adv. Mater. 33 (2021), 2105135.

[21] S. Chen, B. Wang, J. Zhu, L. Wang, H. Ou, Z. Zhang, X. Liang, L. Zheng, L. Zhou, Y. Su, D. Wang, Y. Li, Lewis acid site-promoted single-atomic Cu catalyzes electrochemical $CO_2$ methanation, Nano Lett. 21 (2021) 7325–7331.

[22] S. Sun, Q. An, W. Wang, L. Zhang, J. Liu, W. Goddard, Efficient photocatalytic reduction of dinitrogen to ammonia on bismuth monoxide quantum dots, J. Mater. Chem. A 5 (2017) 201–209.

[23] K. Feng, S. Wang, D. Zhang, L. Wang, Y. Yu, K. Feng, Z. Li, Z. Zhu, C. Li, M. Cai, Z. Wu, N. Kong, B. Yan, J. Zhong, X. Zhang, G.A. Ozin, L. He, Cobalt plasmonic superstructures enable almost 100% broadband photon efficient $CO_2$ photocatalysis, Adv. Mater. 32 (2020) 2000014.

[24] L. Cheng, X. Yue, J. Fan, Q. Xiang, Site-specific electron-driving observations of $CO_2$-to-$CH_4$ photoreduction on Co-doped $CeO_2$/crystalline carbon nitride S-scheme heterojunctions, Adv. Mater. 34 (2022), 2200929.

[25] F. Wang, K. Zhou, X. Liang, X. Zhou, D. Duan, C. Ge, X. Zhang, Y. Shi, H. Lin, Q. Zhu, L. Li, H. Hu, H. Zhang, Revealing size-dependency of ionic liquid to assist perovskite film formation mechanism for efficient and durable perovskite solar cells, Small Methods doi: 10.1002/smtd.202300210.

[26] G. Kresse, J. Furthmüller, Efficiency of ab-initio total energy calculations for metals and semiconductors using a plane-wave basis set, Comp. Mater. Sci. 6 (1996) 15–50.

[27] G. Kresse, J. Furthmüller, Efficient iterative schemes for ab initio total-energy calculations using a plane-wave basis set, Phys. Rev. B 54 (1996) 11169–11186.

[28] J.P. Perdew, K. Burke, M. Ernzerhof, Generalized gradient approximation made simple, Phys. Rev. Lett. 77 (1996) 3865–3868.

[29] G. Kresse, D. Joubert, From ultrasoft pseudopotentials to the projector augmented-wave method, Phys. Rev. B 59 (1999) 1758–1775.

[30] P.E. Blöchl, Projector augmented-wave method, Phys. Rev. B 50 (1994) 17953–17979.

[31] Y. Tong, H. Guo, D. Liu, X. Yan, P. Su, J. Liang, S. Zhou, J. Liu, G. Lu, S. Dou, Vacancy engineering of iron-doped $W_{18}O_{49}$ nanoreactors for low-barrier electrochemical nitrogen reduction, Angew. Chem. Int. Ed. 59 (2020) 7356–7361.

[32] P. Xin, J. Li, Y. Xiong, X. Wu, J. Dong, W. Chen, Y. Wang, L. Gu, J. Luo, H. Rong, C. Chen, Q. Peng, D. Wang, Y. Li, Revealing the active species for aerobic alcohol oxidation by using uniform supported palladium catalysts, Angew. Chem. Int. Ed. 57 (2018) 4642–4646.

[33] C. Liang, H. Niu, H. Guo, C. Niu, Y. Yang, H. Liu, W. Tang, H. Feng, Efficient photocatalytic nitrogen fixation to ammonia over bismuth monoxide quantum dots-modified defective ultrathin graphitic carbon nitride, Chem. Eng. J. 406 (2021), 126868.

[34] C. Gao, S. Chen, Y. Wang, J. Wang, X. Zheng, J. Zhu, L. Song, W. Zhang, Y. Xiong, Heterogeneous single-atom catalyst for visible-light-driven high-turnover $CO_2$ reduction: The role of electron transfer, Adv. Mater. 30 (2018), 1704624.

[35] W. Cheng, H. Su, F. Tang, W. Che, Y. Huang, X. Zheng, T. Yao, J. Liu, F. Hu, Y. Jiang, Q. Liu, S. Wei, Synergetic enhancement of plasmonic hot-electron injection in Au cluster-nanoparticle/$C_3N_4$ for photocatalytic hydrogen evolution, J. Mater. Chem. A 5 (2017) 19649–19655.

[36] Z. Dai, F. Qin, H. Zhao, J. Ding, Y. Liu, R. Chen, Crystal defect engineering of aurivillius $Bi_2MoO_6$ by Ce doping for increased reactive species production in photocatalysis, ACS Catal. 6 (2016) 3180–3192.

[37] W. Shao, S. Wang, J. Zhu, X. Li, X. Jiao, Y. Pan, Y. Sun, Y. Xie, In-plane heterostructured $Ag_2S$-$In_2S_3$ atomic layers enabling boosted $CO_2$ photoreduction into $CH_4$, Nano Res 12 (2017) 4520–4527.

[38] Y. Luo, B. Deng, Y. Pu, A. Liu, J. Wang, K. Ma, F. Gao, B. Gao, W. Zou, L. Dong, Interfacial coupling effects in g-$C_3N_4$/$SrTiO_3$ nanocomposites with enhanced $H_2$ evolution under visible light irradiation, Appl. Catal. B: Environ. 247 (2019) 1–9.

[39] Y. Xu, J. Long, L. Tu, W. Dai, L. Yang, J. Zou, X. Luo, CoO engineered $Co_9S_8$ catalyst for $CO_2$ photoreduction with accelerated electron transfer endowed by the built-in electric field, Chem. Eng. J. 426 (2021) 131849.

[40] X. Jiao, Z. Chen, X. Li, Y. Sun, S. Gao, W. Yan, C. Wang, Q. Zhang, Y. Lin, Y. Xie, Defect-mediated electron-hole separation in one-unit-cell $ZnIn_2S_4$ layers for boosted solar-driven $CO_2$ reduction, J. Am. Chem. Soc. 139 (2017) 7586–7594.

[41] D. Wheeler, J. Zhang, Exciton dynamics in semiconductor nanocrystals, Adv. Mater. 25 (2013) 2878–2896.

[42] J. Huang, Q. Shang, Y. Huang, F. Tang, Q. Zhang, Q. Liu, S. Jiang, F. Hu, W. Liu, T. Yao, Y. Jiang, Z. Pan, Z. Sun, S. Wei, Oxyhydroxide nanosheets with highly efficient electron-hole pair separation for hydrogen evolution, Angew. Chem. Int. Ed. 55 (2016) 2137–2141.

[43] H. Ma, X. Li, S. Fan, Z. Yin, G. Gan, M. Qin, P. Wang, Y. Li, L. Wang, In situ formation of interfacial defects between Co-based spinel/carbon nitride hybrids for efficient $CO_2$ photoreduction, ACS Appl. Energy Mater. 3 (2020) 5083–5094.

[44] Z. Miao, Y. Zhang, N. Wang, P. Xu, X. Wang, BiOBr/$Bi_2S_3$ heterojunction with S-scheme structure and oxygen defects: in-situ construction and photocatalytic behavior for reduction of $CO_2$ with $H_2O$, J. Colloid Interf. Sci. 620 (2022) 407–418.

[45] X. Jin, Y. Xu, X. Zhou, C. Lv, Q. Huang, G. Chen, H. Xie, T. Ge, J. Cao, J. Zhan, L. Ye, Single-atom Fe triggers superb $CO_2$ photoreduction on a bismuth-rich catalyst, ACS Mater. Lett. 3 (2021) 364–371.

[46] Q. Meng, C. Lv, J. Sun, W. Hong, W. Xing, L. Qiang, G. Chen, X. Jin, High-efficiency Fe-Mediated $Bi_2MoO_6$ nitrogen-fixing photocatalyst: Reduced surface work function and ameliorated surface reaction, Appl. Catal. B: Environ. 256 (2019), 117781.

[47] X. Wang, Z. Zhang, Z. Huang, P. Dong, X. Nie, Z. Jin, X. Zhang, Synergistic effect of N-Ho on photocatalytic $CO_2$ reduction for N/Ho co-doped $TiO_2$ nanorods, Mater. Res. Bull. 118 (2019) 110502.

[48] W. Xie, K. Li, X. Liu, X. Zhang, H. Huang, P-mediated Cu–N4 sites in carbon nitride realizing $CO_2$ photoreduction to $C_2H_4$ with selectivity modulation, Adv. Mater. 35 (2023), 2208132.

[49] C. Pan, G. Bian, Y. Zhang, Y. Lou, Y. Zhang, Y. Dong, J. Xu, Y. Zhu, Efficient and stable $H_2O_2$ production from $H_2O$ and $O_2$ on $BiPO_4$ photocatalyst, Appl. Catal. B: Environ. 316 (2022), 121675.

[50] A.N. Baga, G.R.A. Johnson, N.B. Nazhat, R.A. Saadalla-Nazhat, A simple spectrophotometric determination of hydrogen peroxide at low concentrations in aqueous solution, Anal. Chim. Acta 204 (1988) 349–353.

[51] J. Kolle, M. Fayaz, A. Sayari, Understanding the effect of water on $CO_2$ adsorption, Chem. Rev. 121 (2021) 7280–7345.

[52] B. Hammer, J.K. Nørskov, Advances in Catalysis, Vol. 45, Academic Press, 2000, pp. 71–129.

[53] Q. Wang, C. Cai, M. Dai, J. Fu, X. Zhang, H. Li, H. Zhang, K. Chen, Y. Lin, H. Li, J. Hu, M. Miyauchi, Recent advances in strategies for improving the performance of $CO_2$ reduction on single atom catalysts, Small Sci. 1 (2021), 2000028.

[54] L. Shi, P. Wang, Q. Wang, X. Ren, F. Lchihara, W. Zhou, H. Zhang, Y. Lzumi, B. Cao, S. Wang, H. Chen, J. Ye, Efficient photocatalytic $CO_2$ reduction mediated by transitional metal borides: Metal site-dependent activity and selectivity, J. Mater. Chem. A 8 (2020) 21833–21841.

[55] Y. Yu, X. Dong, P. Chen, Q. Geng, H. Wang, J. Li, Y. Zhou, F. Dong, Synergistic effect of Cu single atoms and Au−Cu alloy nanoparticles on $TiO_2$ for efficient $CO_2$ photoreduction, ACS Nano 15 (2021) 14453–14464.

[56] W. Bi, Y. Hu, H. Jang, L. Zhang, C. Li, Revealing the sudden alternation in Pt@h-BN nanoreactors for nearly 100% $CO_2$-to-$CH_4$ photoreduction, Adv. Funct. Mater. 31 (2021), 2010780.

[57] P. Liu, Z. Huang, X. Gao, X. Hong, J. Zhu, G. Wang, Y. Wu, J. Zeng, X. Zheng, Synergy between palladium single atoms and nanoparticles via hydrogen spillover foe enhancing $CO_2$ photoreduction to $CH_4$, Adv. Mater. 34 (2022), 2200057.

[58] M. Ma, Z. Huang, D. Doronkin, W. Fa, Z. Rao, Y. Zou, R. Wang, Y. Zhong, Y. Cao, R. Zhang, Y. Zhou, Ultrahigh surface density of Co-$N_2$C single-atom-sites for boosting photocatalytic $CO_2$ reduction to methanol, Appl. Catal. B: Environ. 300 (2022), 120695.

[59] S. Ji, Y. Qu, T. Wang, Y. Chen, G. Wang, X. LI, J. Dong, Q. Chen, W. Zhang, Z. Zhang, S. Liang, R. Yu, Y. Wang, D. Wang, Y. Li, Rare-earth single erbium atoms for enhanced photocatalytic $CO_2$ reduction, Angew. Chem. Int. Ed. 59 (2020) 10651–10657.